A Low-Profile and High-Gain Frequency Beam Steering Subterahertz Antenna Enabled by Silicon Micromachining

Adrian Gomez-Torrent, *Graduate Student Member, IEEE*, María García-Vigueras, *Member, IEEE*, Laurent Le Coq, Adham Mahmoud, Mauro Ettorre, *Senior Member, IEEE*, Ronan Sauleau, *Fellow, IEEE*, and Joachim Oberhammer, *Senior Member, IEEE*

***Abstract*— A very low-profile sub-THz high-gain frequency beam steering antenna, enabled by silicon micromachining, is reported for the first time in this paper. The operation bandwidth of the antenna spans from 220 to 300 GHz providing a simulated field of view of 56°. The design is based on a dielectric filled PPW leaky-wave antenna fed by a pillbox. The pillbox, a two-level PPW structure, has an integrated parabolic reflector to generate a planar wave front. The device is enabled by two extreme aspect ratio, 16 x 16 mm large perforated membranes, which are only 30 μm thick, that provide the coupling between the two PPWs and form the LWA. The micromachined low-loss PPW structure results in a measured average radiation efficiency of −1 dB and a maximum gain of 28.5 dBi with an input reflection coefficient below −10 dB. The overall frequency beam steering frontend is extremely compact (24 x 24 x 0.9 mm) and can be directly mounted on a standard WM-864 waveguide flange. The design and fabrication challenges of such high performance antenna in the sub-THz frequency range are described and the measurement results of two fabricated prototypes are reported and discussed.**

***Index Terms*— Beam steering, leaky-wave antennas (LWAs), silicon micromachining, silicon on insulator, submillimeter-wave antennas, terahertz radiation, quasi-optics.**

Manuscript received May 7, 2019; revised August 1, 2019; accepted August 31, 2019. Date of publication September 30, 2019; date of current version February 3, 2020. This work was supported in part by the European Research Council (ERC) through the contribution of Kungliga Tekniska Högskolan under the European Union's Horizon 2020 Research and Innovation Programme under Grant 616846, in part by the Swedish Foundation for Strategic Research Synergy Grant Electronics under Grant SE13-007, in part by the European Union through the European Regional Development Fund (ERDF) under the contribution of the Institut d'Électronique et de Télécommunications de Rennes (IETR), and in part by the French Region of Brittany, Ministry of Higher Education and Research, Rennes Métropole and Conseil Départemental 35, through the CPER Project SOPHIE/STIC & Ondes. *(Corresponding author: Adrian Gomez-Torrent.)*

A. Gomez-Torrent and J. Oberhammer are with the Division of Micro and Nanosystems, School of Electrical Engineering and Computer Science, Kungliga Tekniska Högskolan (KTH) Royal Institute of Technology, 100 44 Stockholm, Sweden (e-mail: adriango@kth.se).

M. García-Vigueras is with the Institut National des Sciences Appliquées de Rennes, 35708 Rennes, France.

L. Le Coq, A. Mahmoud, M. Ettorre, and R. Sauleau are with the CNRS, Institut d'Électronique et de Télécommunications de Rennes (IETR) - UMR 6164, University of Rennes 1, 35000 Rennes, France.

Color versions of one or more of the figures in this article are available online at http://ieeexplore.ieee.org.

Digital Object Identifier 10.1109/TAP.2019.2943328

I. Introduction

THE availability of radio frequency systems working at sub-THz frequencies (from 100 GHz up to 1 THz) has been increasing in the last years due to technological advances improving the performance of both passive waveguide components [1] and active circuits [2] in this frequency range.

At the same time, the development of high-performance RF components in the sub-THz region enables new applications that can exploit the large bandwidth available at such high frequency, or the highly-miniaturized RF front-ends resulting from the reduced wavelength. Radar systems are one of the applications that can benefit from going to higher frequencies due to the achievable high resolution and the interactions that electromagnetic waves have with different materials as the frequency increases [3]. Even if solutions for radars exist at lower frequencies providing high-gain, low side-lobe levels (SLLs), and beam steering capabilities, their scaling to sub-THz frequencies implies many technological challenges.

A commonly used antenna for high frequency radar applications is a reflector fed by a horn due to its excellent performance and commercial availability [4], [5]. Their main drawback is the high volume and mass, as well as the need for moving mirrors or stages in order to achieve beam scanning. Moreover, more advanced feeds such as spline profile horns [6], multiflare angle horns [7] or corrugated horns [8] require a more complex fabrication process, which becomes challenging when approaching submillimeter-wave frequencies.

Integrated lens antennas (ILAs) can be a good alternative for applications requiring high gain in the sub-THz frequency range [9]. ILAs provide a more compact solution than traditional optical systems since the source is in direct contact with the substrate of the lens antenna. Konstantinidis *et al.* [10] reported on a computer numerical control (CNC)-milled hyperhemispherical lens antenna fed by an open-ended waveguide for radar applications. ILAs can be also implemented at much higher frequencies as shown by del Pino *et al.* [11], where they developed a 1.9 THz ILA. The silicon lens was micromachined and required a total amount of 13 wafers for the lower gain version (32 dBi). The same authors recently demonstrated beam steering capabilities with a similar design

at 550 GHz [12], however, the presented solution requires movement of the lens by external mechanics, which increases the overall complexity, cost, and volume of the system.

Frequency scanned antennas have been shown as a good alternative to mechanically scanned systems due to their lower cost, size, and complexity. Although they cannot provide the entire bandwidth at each individual direction in space, they allow to scan the beam in one direction by changing the working frequency, thus becoming a good solution when compactness is a priority and the required range resolution is not high. Such systems can be implemented by true-time-delay (TTD) lines or leaky-wave antennas (LWAs), for example, and their use for sub-THz radar applications was demonstrated in the WM864 band by Murano *et al.* [13]. The authors used a periodically loaded microstrip LWA that generates a fan-shaped beam scanning in elevation. However, a narrow beam both in azimuth and elevation would require the use of an additional beam forming network (BFN). BFNs tend to be electrically long and would considerably decrease the radiation efficiency of the antenna at sub-THz frequencies if implemented in microstrip technology.

The rather complex topology of BFNs for high gain and beam steering antennas limits their implementation to waveguide technology at sub-THz frequencies, since any planar transmission line technology generates excessive loss. Some work has been done in developing substrate integrated waveguide (SIW) planar antennas in order to simplify the fabrication process by using printed circuit board (PCB) technology [14]–[16]. But the biggest limitations of PCB-based SIW components are still the increased loss, the available substrate thickness, and via geometries, that typically limit the maximum operation frequency of these systems below 100 GHz.

Quasi-optical BFNs can be a good alternative to classical BFNs. They can deliver compact, directive, and low loss antennas, but its implementation at sub-THz frequencies becomes challenging and all previous demonstrations were done in PCB [14], [16], LTCC [17], or CNC-milling [18], [19]. The works in [16]–[18] are based on pillbox designs, a topology that was first introduced by Rotman [20] and it is a particular case of *quasi*-optical BFNs.

Silicon micromachining has been an enabling technology for low-loss waveguide components at sub-THz frequencies [1], [12], [21]–[23]. Some of the advantages of silicon micromachining are the ability to fabricate features down to the micron scale, batch production, better tolerances, and better batch-to-batch uniformity. However, little work has been done in using silicon micromachining for complex antenna BFNs. Tekkouk *et al.* reported on a 350 GHz silicon micromachined corporate feed antenna [24], achieving a 29.5 dBi gain at the center frequency for a single beam at broadside. However, the measured gain was over 3 dB lower than expected, and the authors attributed it to fabrication nonidealities.

Sarabandi *et al.* [25] recently demonstrated a frequency beam-steering antenna in the WM864 band using true time delay lines. The long lines required to implement the TTD BFN generating the steering of the beam are implemented in a silicon micromachined waveguide technology to minimize the insertion loss and avoid long-waveguide effects. The directivity in the plane orthogonal to the beam steering is achieved by series-fed patch antenna arrays, which gives a total gain of 29 dBi but in a narrow 6% fractional bandwidth due to the serial feed topology in both BFNs. Such narrow bandwidths on antennas with large frequency scanning ranges fail to provide instantaneous bandwidth on a given direction in space due to the large beam squinting, which can be an issue when using them for communications or radar applications.

In this work, we present for the first time a beam steering front-end working at sub-THz frequencies based on a LWA fed by an integrated *quasi*-optical BFN. The antenna has a 80 GHz operation bandwidth and a center frequency of 260 GHz, with a simulated beam steering between $-75.6°$ and $-19.4°$ in elevation from broadside. The *quasi*-optical BFN reported here represents the first hollow waveguide pillbox structure in the sub-THz range, and is enabled by silicon micromachining. The specific design considerations for the fabrication of such antenna in the sub-THz frequency range are described and the characterization of two manufactured prototypes is presented.

II. Antenna Structure and Design

The antenna can be divided into two main components: the radiation part, a dielectric-filled parallel plate waveguide (PPW) loaded with periodic slots forming a LWA; and the *quasi*-optical hollow PPW BFN, namely a pillbox structure. The shape of the beam in azimuth is determined by the illumination of the parabola (in the x-axis), and the shape of the beam in elevation is determined by the illumination of the aperture by the LWA (in the y-axis), where the combination of both results in a pencil shaped beam. The antenna is fabricated by silicon-micromachining, as described in Section III.

A schematic drawing of the device is shown in Fig. 1. Two of the three chips required for its assembly have high aspect ratio (AR) membranes of 16x 16x 0.03 mm (AR > 530:1), which make their fabrication very challenging and where the mono-crystalline structure of the silicon wafers is a requirement for the membranes not to break. In addition, silicon micromachining allows for accurate perforations in these membranes, which are used for coupling between the PPW layers and for the LWA radiation.

Fig. 1 also illustrates the wave propagation from the feeding point towards free space. The H-plane sectoral horn in chip 2 launches a cylindrical wave that illuminates a parabolic reflector and is coupled as a plane wave to chip 1, where is radiated by the LWA.

The final device consists of a stack of 3 chips, which was found to be the minimum needed to implement such system. These chips are completely metallized with gold, as described in Section III, and the electromagnetic waves do not interact with the silicon or silicon oxide, that are structural materials. Each chip has a specific function that will be described in this section. For the LWA, an additional perforated dielectric layer has to be inserted to avoid unwanted radiation beams.

The commercial software CST Studio was used for the electromagnetic simulations in this paper, where conductor and dielectric loss, surface roughness, and geometrical fabrication

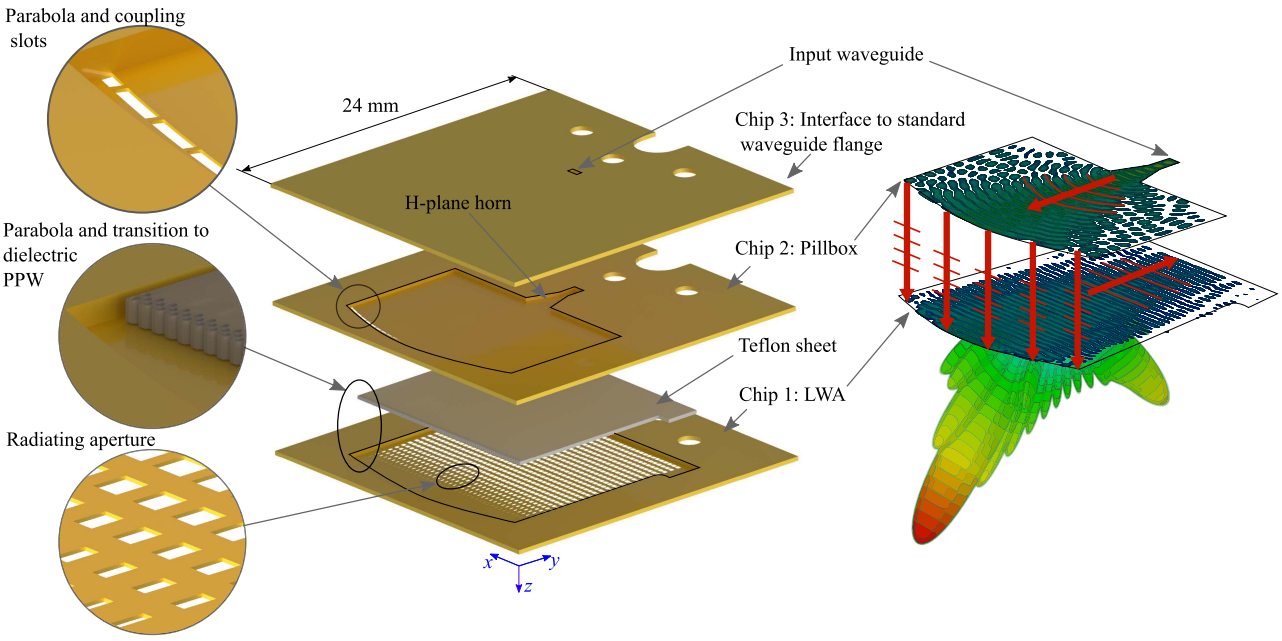

Fig. 1. CAD drawing of the antenna assembly showing the three-chip structure and the integrated dielectric substrate. Right part of the figure shows a conceptual representation of the field propagation from chip 2 (cylindrical wave front) to chip 3 (planar wave front) through the coupling slots and radiation diagram at 260 GHz.

imperfections have been taken into account in the simulation model.

A. Chip 1: Leaky-Wave Antenna

The LWA in chip 1 is based on a PPW loaded with a periodic slot array on the top plate, generating an unbound mode that radiates into free space [26]. The mode propagating in the PPW is a *quasi*-transverse electromagnetic (TEM) mode generated by the pillbox, however, a pure TEM mode can be considered for the initial antenna calculations

$$\beta_y = \frac{2\pi}{\lambda_0}\sqrt{\epsilon_r} \tag{1}$$

$$k_{y,n} = \left(\beta_y + \frac{2\pi}{d}n\right) - j\alpha \tag{2}$$

$$sin(\theta_n) \approx \beta_{y,n}/k_0. \tag{3}$$

The propagation constant, β_y, of the unloaded PPW can be written as in (1), where λ_0 is the free-space wavelength, and ϵ_r is the relative dielectric permittivity of the media inside the PPW. The dispersion diagram of such a structure loaded with periodic slots (2) forming a LWA is shown in Fig. 2 for a Teflon-filled PPW, where d is the period of the slots and n the index of the Floquet harmonic. The insertion of a dielectric medium in the micromachined PPW structure is a straightforward solution to avoid the radiation of the $n = 0$ harmonic, since the LWA is designed to have a beam from the $n = -1$ harmonic scanning from backfire to broadside (3).

The PPW height and dielectric material are set by the fabrication constrains, and their selection criteria will be further discussed in Section III. The period of the slots defines the scanning of the beam, as provided by (3), and is fixed to

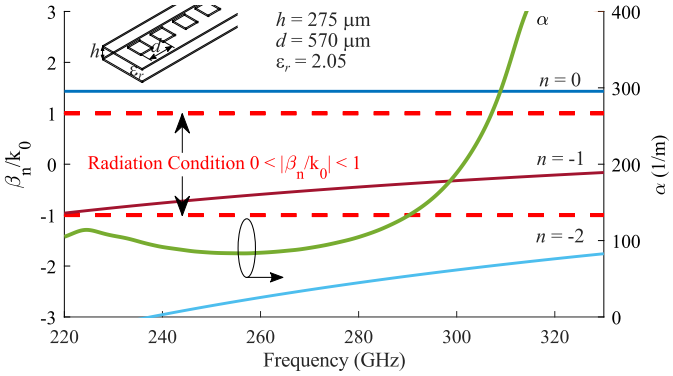

Fig. 2. Dispersion diagrams for a periodically slotted PPW, showing the propagation constant (β_n) normalized to the free-space wavenumber (k_0) and the attenuation constant (α). Data extracted from full-wave simulations of the loaded PPW structure.

570 μm for a beam scanning from backfire to broadside in the band of interest.

The most relevant dimensions of the antenna are shown in Fig. 3 and Table I. The aperture size was set to 14x 16 mm for a directivity of 30 dBi at a center frequency of 260 GHz. The size of the slots and the period in the x direction were set for a radiation efficiency around 80%, see Fig. 4. This radiation efficiency takes into account the mismatching in the input waveguide port of the device as well as the conductor and dielectric loss.

The transition between the hollow PPW and the slotted dielectric PPW is shown in Fig. 3. First, a perforated section in the dielectric substrate of length $\lambda/4$ makes the transition between air and dielectric media in the PPW. The diameter of the holes is smaller than $\lambda/10$ at the highest frequency and the transition is made before the LWA starts, which avoids

TABLE I
DIMENSIONS OF PPW TO LWA TRANSITION

Parameter	Description	Value
ϵ_r	Teflon relative dielectric constant*	2.05
$tan(\delta)$	Teflon loss tangent*	$4.5{\cdot}10^{-4}$
th	Teflon layer thickness	250 µm
h	Height of the parallel plate waveguide	275 µm
ϕ	Hole diameter	100 µm
$\lambda/4$	Length of air to dielectric transition	300 µm
w	Slot width	300 µm
l	Slot length	330 µm
$l_1 - l_6$	Slot length linear taper	50 – 330 µm
d	Slot period in propagation axis	570 µm
d_x	Slot period in x axis (transversal)	400 µm

* Measured at 18 GHz by manufacturer

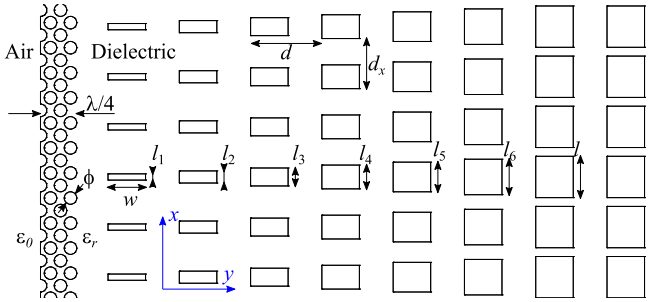

Fig. 3. Schematic drawing of the transition between hollow PPW and slotted dielectric PPW. Relevant dimensions are shown in Table I.

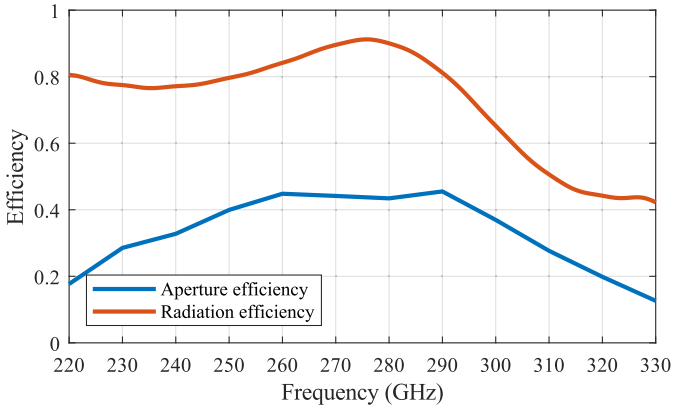

Fig. 4. Simulated radiation efficiency and aperture efficiency for the LWA. The radiation efficiency includes antenna mismatching, conductor loss, and dielectric loss. The aperture efficiency compares the maximum theoretical directivity of the antenna, given the aperture size, with the simulated directivity including the amplitude tapering in both planes.

any phase aberrations. The transition between the dielectric PPW and the slotted waveguide is implemented by linearly increasing the length of the slots from 50 µm to 330 µm using a six-slot taper.

B. Chip 2: Pillbox Beam Forming Network

The pillbox is the integrated *quasi*-optical BFN that generates a planar TEM wave-front in the upper PPW in chip 3 from a cylindrical TEM mode launched by the H-plane horn

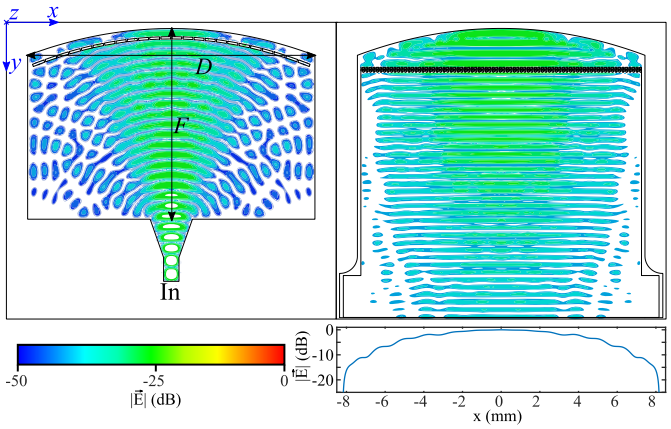

Fig. 5. E-field representation of the *quasi*-optical BFN in both PPW waveguides, and E-field amplitude tapering in the direction perpendicular to the wave propagation. F and D represent the focal distance and diameter of the parabolic reflector, respectively.

in the lower PPW in chip 2, as shown in Fig. 5. The E-field amplitude profile in Fig. 5 represents the edge tapering on the parabolic reflector, which is -15 dB with respect to the center of the parabola, and controls the SLL of the radiation pattern in the H-plane of the antenna.

The diameter and focal distance of the parabolic reflector are 16.4and 11 mm, respectively, ($F/D = 0.67$). The dimensions of the slots for the transition between the two PPWs vary from 563x 123.5 µm in the center of the reflector to 689x 132 µm on the edges. A more detailed description of the pillbox BFN and in-depth design procedure can be found in the literature [16], [18], [20].

C. Chip 3: Chip-to-Flange Interface

Chip 3, as shown in Fig. 1, is used as an interface between the in-plane silicon micromachined rectangular hollow metallic waveguide in chip 2, and the standard UG-387 waveguide flange. The chips contain holes for the alignment pins and screws, which enable a direct connection to the waveguide flange without any additional test fixtures or interfaces. This direct-mount technique is superior to alternative setups using CNC-milled transitions or test fixtures as described in [22] and [24], due to the lower accuracy generally achieved by the CNC-milling process that drastically reduces the performance of the antenna or device under test.

The alignment holes in chip 1 are photolithographically defined, i.e., with micrometer-accuracy, to tightly fit the pins of a standard waveguide flange. In addition, an increased repeatability and accuracy is achieved by using elliptical alignment holes as described by Campion *et al.* [27]. The holes are designed for an alignment accuracy better than 5 µm, which is far superior to the standard flange-to-flange mounting accuracy of 25 µm.

The input waveguide dimensions are 864x 432 µm and a stepped impedance matching section is included in the chip to minimize the reflections between the standard waveguide and the reduced height waveguide used in the rest of the device. The height of the waveguide is 275 µm, chosen as

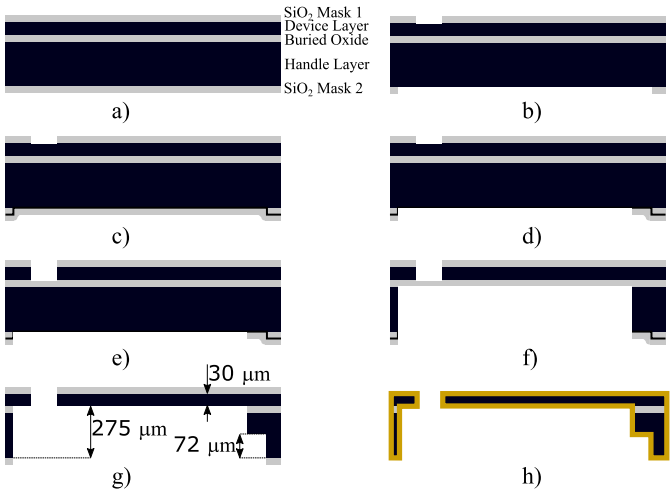

Fig. 6. Fabrication process flow shown with a cross section of the chip 2, not to scale. (a) Initial SOI wafer. (b) patterning of masks 1 and 2. (c) PECVD deposition of SiO_2 layer for mask 3. (d) patterning of mask 3. (e) DRIE of device layer. (f) DRIE of handle layer (first step through BOX). (g) DRIE of handle layer (second step, 72 μm deep). (h) SiO_2 removal and sputtering of 2 μm of gold.

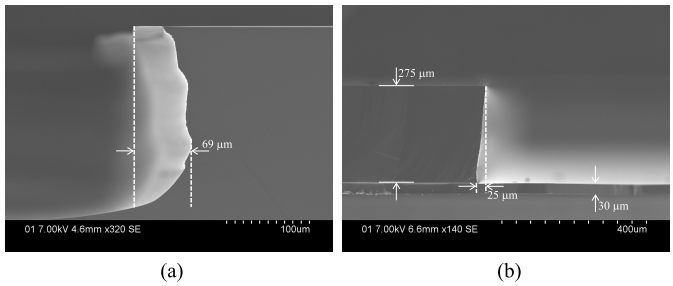

Fig. 7. Cross-section SEM image of the sidewall of a PPW cavity using (a) a standard Bosch process. (b) Modified recipe optimized for etching large trenches.

a tradeoff between etching performance and electromagnetic performance. The height of the matching step is set to 203 μm and is calculated using the Trust Region Framework algorithm [28], a local linear optimization algorithm implemented in the simulation software CST.

III. Fabrication

Two antenna prototypes were fabricated in separate batches using the silicon on insulator (SOI)-wafer micromachining process at Kungliga Tekniska Högskolan (KTH) Electrumlab, Stockholm. The use of SOI wafers as a substrate is critical for the fabrication of the stacked-PPW structures at these high frequencies due to the thin layers required to form the coupling slots and the LWA. The SOI wafers used for this work have a 275 μm handle layer, a 30 μm device layer, and a 3 μm buried oxide layer (BOX). A simplified process flow is shown in Fig. 6.

The SOI wafers are first wet-thermally oxidized at 1100 °C to form 2 μm oxide layers on both sides of the wafers. These layers are patterned by photolithography and dry etching to form the hard masks Mask 1 and Mask 2, see Fig. 6 (a) and (b). A 2 μm plasma enhanced physical vapor deposition (PECVD) silicon oxide layer is deposited on the handle layer completely

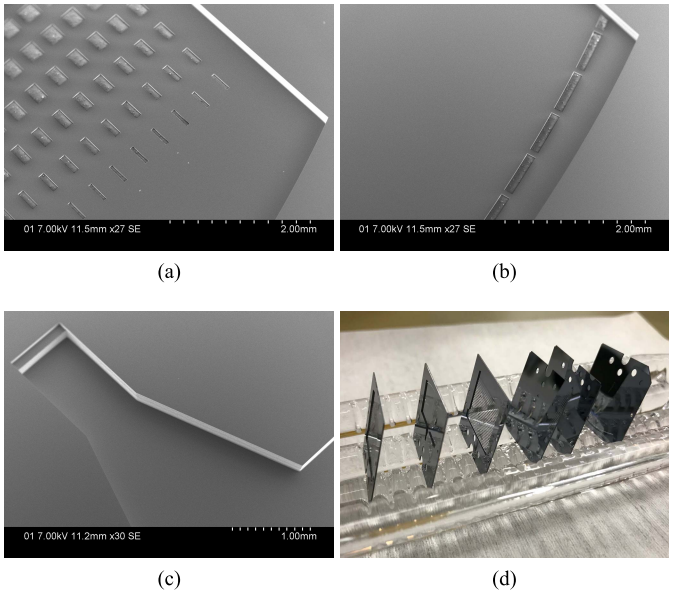

Fig. 8. SEM images of fabricated devices showing (a) LWA slots and reflector in chip 1. (b) Coupling slots and reflector in chip 2. (c) Input waveguide horn antenna with stepped E-plane bend in chip 2. (d) Picture of the fabricated chips before metallization.

covering Mask 2, which is patterned to form Mask 3. This oxide mask stacking allows to independently etch different heights in the handle layer, which are needed to fabricate impedance matching geometries.

A STS multiplexed ICP system is used for the deep reactive ion etching (DRIE) of the silicon. First, the device layer is etched using a standard 2-step Bosch process. The etching of the handle layer requires a modified etching recipe due to the large open areas being etched to form the PPW cavities, which are 16x 16 mm large. The exothermic nature of the chemical etching of silicon with sulphur hexafluoride (SF_6) makes the wafer overheat, thus inhibiting the polymerization of the octafluorocyclobutane (C_4F_8), which is necessary for keeping the sidewalls of the waveguides in a rectangular angle. Fig. 7(a) shows a scanning electron microscope (SEM) image of a 16x 16 mm cavity etched with a nonoptimized Bosch process, with an underetching of over 40 μm, which would strongly deteriorate the performance of the waveguides.

The modified recipe used for the etching of the handle layer has a longer passivation step, lower chamber pressure and higher platen power for the DC biasing. This recipe achieves an etching with a much lower underetching, as shown in Fig. 7(b), which is acceptable and can be easily compensated during the electromagnetic design of the waveguide components.

After etching the handle layer through Mask 3 the remaining few nanometers of oxide are dry etched to expose Mask 2 and the handle layer is now etched through Mask 2 to a depth of 72 μm. This second etching step from the backside of the wafer defines the steps in the waveguides, and can be controlled with an accuracy better than 5 μm. The silicon micromachined chips are shown with SEM images in Fig. 8(a)–(c). Fig. 8(d) shows the chips after etching and before gold metallization. The chips are finally metallized in a DC sputtering system to a thickness of 2 μm on each side.

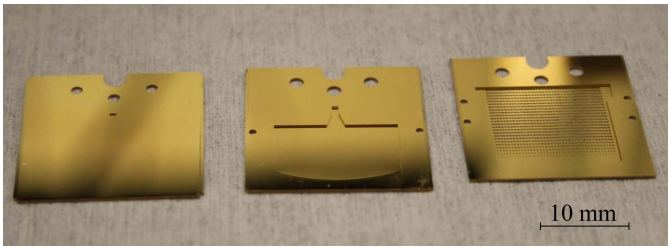

(a)

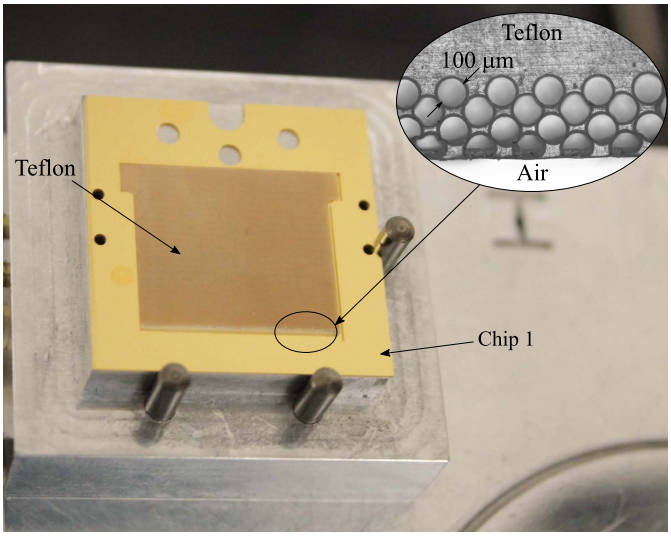

(b)

Fig. 9. Pictures of (a) 3 chips after metallization required to assemble one antenna. (b) CNC-milled Teflon sheet inserted in micromachined chip 1 during assembly process.

The three SOI chips needed for one antenna assembly after metallization are shown in Fig. 9(a).

The Teflon sheet used in the PPW LWA is CNC-milled from a 250 µm thick CuFlon substrate provided by PolyFlon. The contour and the holes for the impedance matching section are machined together with the copper cladding, that is later removed by wet chemical etching. The criteria to select the material to be integrated inside the antenna are: 1) ease of machining, 2) sufficient thermal budget to survive the subsequent gold-to-gold bonding, 3) low loss in the sub-THz frequency range, and 4) low dielectric constant to avoid higher order modes in the PPW and reflections in the air-dielectric interface. The Teflon layer is slightly thinner than the PPW cavity (250 µm thickness as compared to 275 µm cavity height) to avoid any cracking of the membranes during bonding due to the high coefficient of thermal expansion of CuFlon (129 ppm/°C). The lower dielectric substrate thickness was taken into account in all the simulations to predict its influence.

After inserting the Teflon in chip 1, as shown in Fig. 9(b), the remaining chips are stacked and aligned under the microscope before thermal-compression bonding at 200 °C for 1 h. The measured post-bonding alignment accuracy is below 4 µm, as shown by the microscope images of the integrated Vernier scales on the corners of every chip in Fig. 10. These Vernier scales provide alignment resolution of 1 µm and are

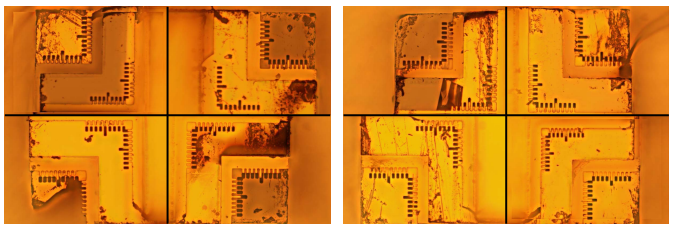

(a) (b)

Fig. 10. Vernier scales showing the chip-to-chip alignment after gold thermal-compression bonding for (a) antenna prototype A#1 and (b) antenna prototype A#2. The typical misalignment in the corner of the chips is 0–2 μm. The maximum misalignment is 4 μm in the top left corner of A#2.

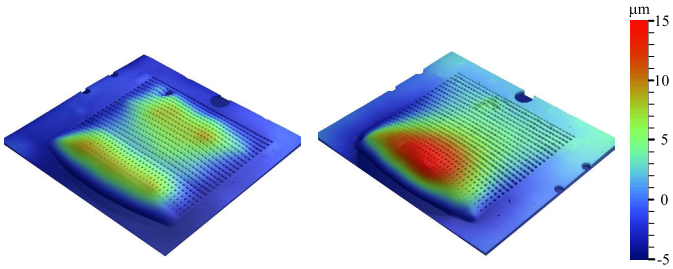

(a) (b)

Fig. 11. Measured membrane deflection in chip 1 for both antenna prototypes showing a maximum of (a) 12.7 μm and (b) 15 μm. Not to scale.

used before bonding for the chip-to-chip alignment and after bonding to check the final alignment accuracy. Such low misalignment errors have no impact on the return loss or insertion loss of the device in this frequency range as demonstrated by the authors in [23].

The deflection of the 30 µm thick membranes used for the PPWs was analysed using a Wyko surface optical profilometer. The stress induced by the relatively thick gold layer is known to bend such membranes due to their large AR. The bending influences the effective height of the PPW, thus having a direct effect on the antenna performance. The optical profilometer data is plotted in Fig. 11, showing the deflection of the membrane in chip 1 for two fabricated antennas. The data shows a maximum offset of 12.7 and 15 µm for the first and second antenna, respectively. The influence of a 15 µm increase in the PPW height was studied in a full wave simulation model, and no significant effects were observed in the antenna performance.

The surface roughness generated by this fabrication process and its effects on the waveguide loss were studied in detail in [21] for this frequency band. The authors demonstrated that the effect of the surface roughness can be modeled by an equivalent gold conductivity that is lower than the theoretical one. A roughness of $R_a = 2.14$ nm in the top and bottom surfaces and $R_a = 163$ nm in the sidewalls can be modeled with an equivalent gold conductivity of $\sigma_{Au} = 1.8 \times 7\ \mathrm{S\,m^{-1}}$, which was used for all the simulations in this work.

IV. Measurement Results

The radiation patterns of two antenna prototypes (in the following referred to as A#1 and A#2) were measured in

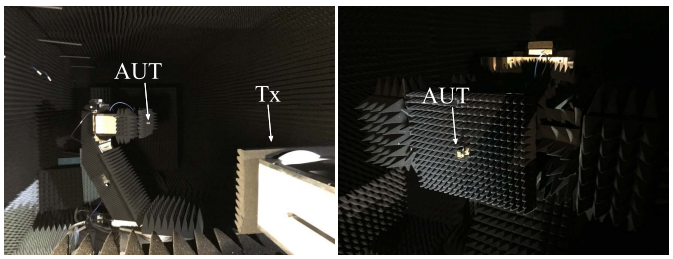

Fig. 12. Antenna radiation pattern far-field measurement setup at IETR.

the millimeter-wave antenna test facility CAMILL at Institut d'Électronique et de Télécommunications de Rennes (IETR). The far-field measurement setup, shown in Fig. 12, based on a classical direct illumination technique, samples the E-field in an elevation over azimuth angular grid that covers the complete upper hemisphere of the antenna under test (AUT). A spherical harmonic expansion is then applied to reconstruct the 3-D radiation pattern at any point, enabling the determination of parameters of interest such as directivity, main beam half power beam-width (HPBW), and pointing angle.

The emission part of the measurement setup is based on a Virginia Diodes (VDI) TxRef frequency extender, mounted on a roll axis and connected to a linearly polarized rectangular horn as a probe. The reception part is based on a VDI Rx frequency extender with a triplexer that allows for the use of only one cable together with rotary joints. The Rx module is mounted on an elevation over roll over azimuth axis. The TxRef and Rx modules are connected to a Keysight VNA N522A and provide a bandwidth from 220 GHz to 330 GHz; however, the radiation measurements were only performed in the 230−290 GHz range due to time limitations. The local oscillator is a Keysight signal generator AG-N5173B.

The AUT design allows for direct mounting on a standard UG-387 flange, as shown in Fig. 13. The direct mounting technique does not require any extra test fixtures or interfaces that are challenging to implement when approaching the THz range [24]. The contact for the connection was visually verified and repeated measurements on the same device show negligible deviations.

The elevation versus frequency plots in Fig. 14 show the measured frequency beam steering behavior of the LWA. The beam steering capability of the antenna can be clearly observed, as well as a back-lobe in the opposite direction from the main lobe. This back-lobe is due to the shorted termination of the PPW after the LWA, i.e., the energy which has not been radiated by the aperture is reflected and travels back in the waveguide in the opposite direction, resulting in radiation in an unwanted direction. This could be solved by increasing the radiation efficiency of the aperture, or by terminating the PPW with a matched load.

The measured E-plane and H-plane radiation patterns, shown in Fig. 15, are in good agreement with the simulation data. The experimental pointing angle and HPBW of the main beam for both antennas are as well coherent with the full-wave simulation results, as shown in Fig. 16. The radiation cut-planes in Fig. 15 and the beam characteristics in Fig. 16 are obtained by using two different sampling grids. The E-plane cuts use an homogeneous elevation/azimuth grid, with the axis of the north/south pole parallel to the optical axis of the chamber and can be directly linked to the 3-D cartography; the H-plane cuts use an homogeneous azimuth/elevation grid, with the axis of the north/south pole perpendicular to the optical axis of the chamber. These two separate sampling grids allow for an antenna analysis based on the 2-D array factor.

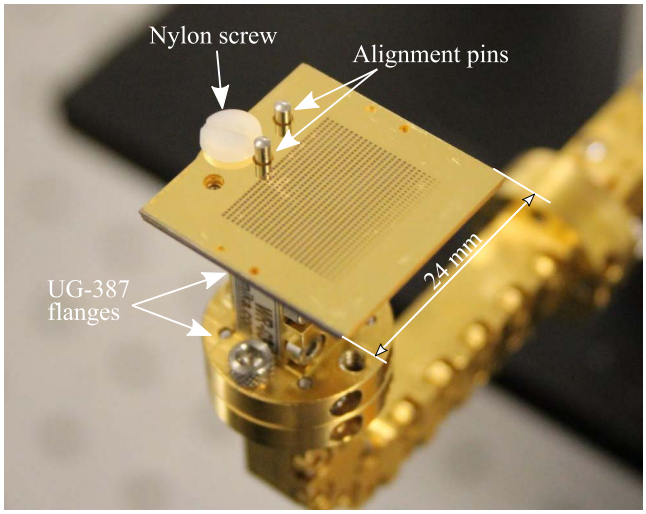

Fig. 13. Antenna prototype mounted on a standard UG-387 waveguide flange using two alignment pins and a nylon UNC 4-40 screw.

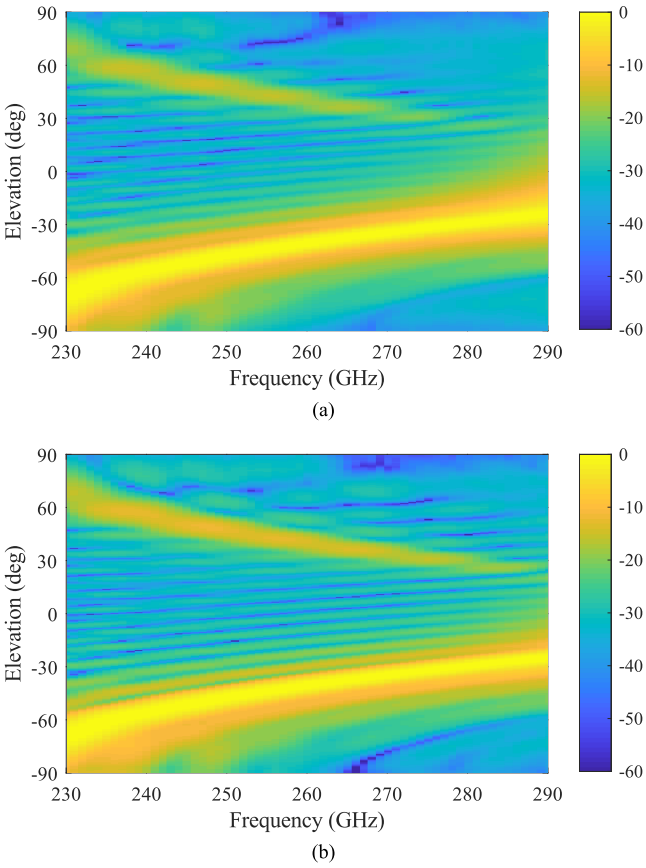

Fig. 14. Measured elevation versus frequency plot showing the normalized radiation pattern for (a) A#1 and (b) A#2.

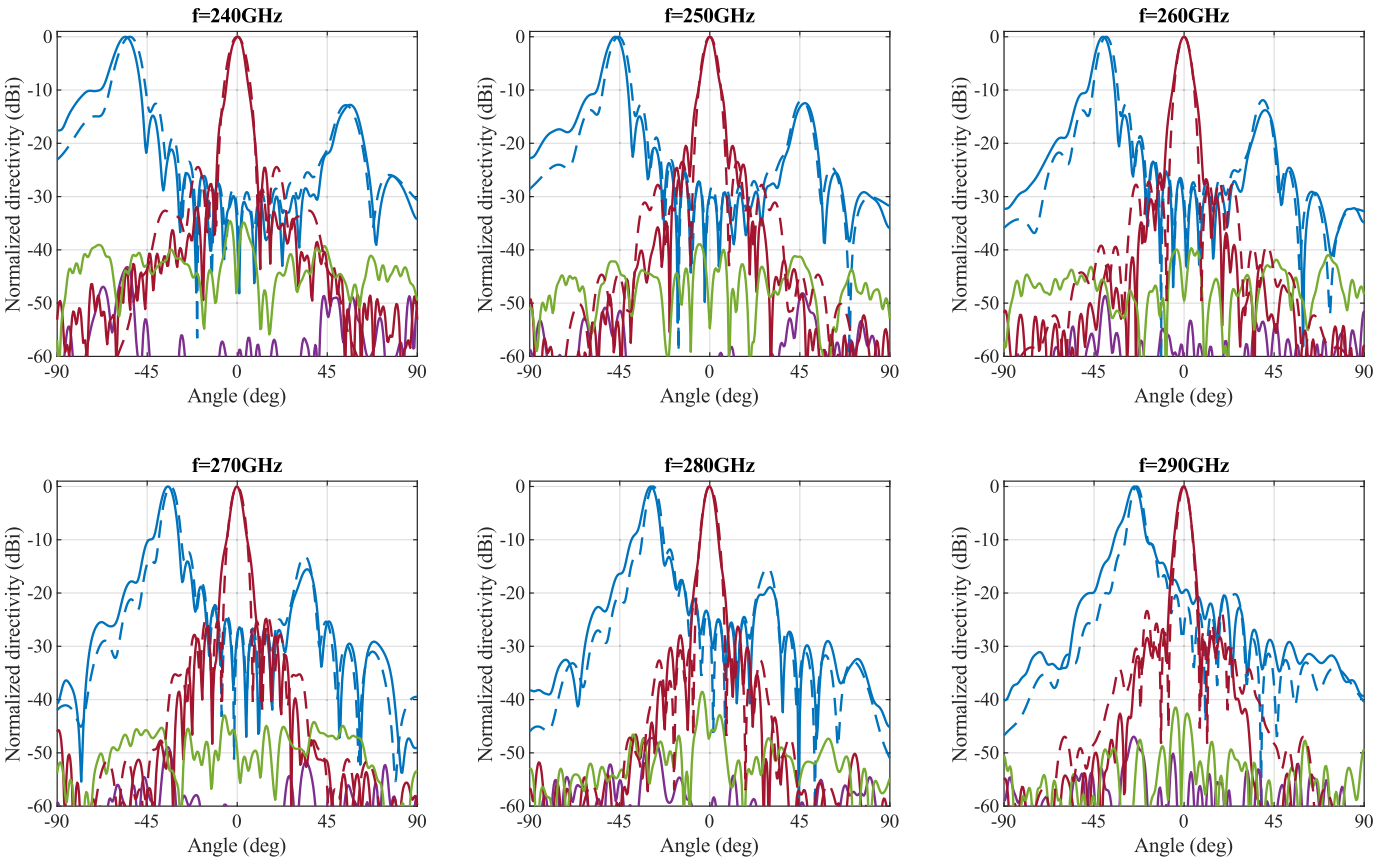

Fig. 15. Measured (solid lines) and simulated (dashed lines) E- and H-plane radiation patterns for A#2 antenna at different frequencies. E-plane cuts are shown with blue lines (coPol) and purple lines (xPol). H-plane cuts are shown with red lines (coPol) and green lines (xPol).

TABLE II
COMPARISON OF SUB-THZ HIGH GAIN ANTENNAS

Reference	Topology	Frequency range (FBW)	Maximum Gain	Total eff. at center freq.	Beam-steering (Scanning range)	Fabrication technology
[6]	Spline diagonal horn	500 – 750 GHz 40 % FBW	21.7 dBi	N.A.	No	CNC-milling
[8]	Corrugated horn	500 – 750 GHz 40 % FBW	31 – 34.5 dBi directivity 1.5 – 4 dB IL	N.A.	No	Stacked rings
[19]	*Quasi*-optical dual reflector	325 – 500 GHz 43 % FBW	32 dBi	−1.8 dB	No	CNC-milling
[10]	Integrated lens antenna	230 – 310 GHz 30 % FBW	30 dBi	−3.8 dB	No	CNC-milling Rexolite
[12]	Integrated lens antenna	500 – 750 GHz 15 % FBW	27 dBi	−1 dB	Mechanical −11 – 16.5°	Silicon micromachining
[16]	LWA fed by pillbox BFN	74 – 78 GHz 5 % FBW	24 dBi	−3 dB	Frequency scanning −50 – −38°	PCB Rogers 5880
[24]	Corporate feed array	335 – 380 GHz 12 % FBW	30 dBi	−3.5 dB	No	Silicon micromachining
[25]	TTD BFN patch antenna array	230 – 245 GHz 6 % FBW	29 dBi	−2.6 dB	Frequency scanning −25 – 25°	Silicon micromachining
This work	LWA fed by pillbox BFN	220 – 300 GHz 30 % FBW	28.5 dBi	−1.2 dB	Frequency scanning −75 – −30°	Silicon Micromachining

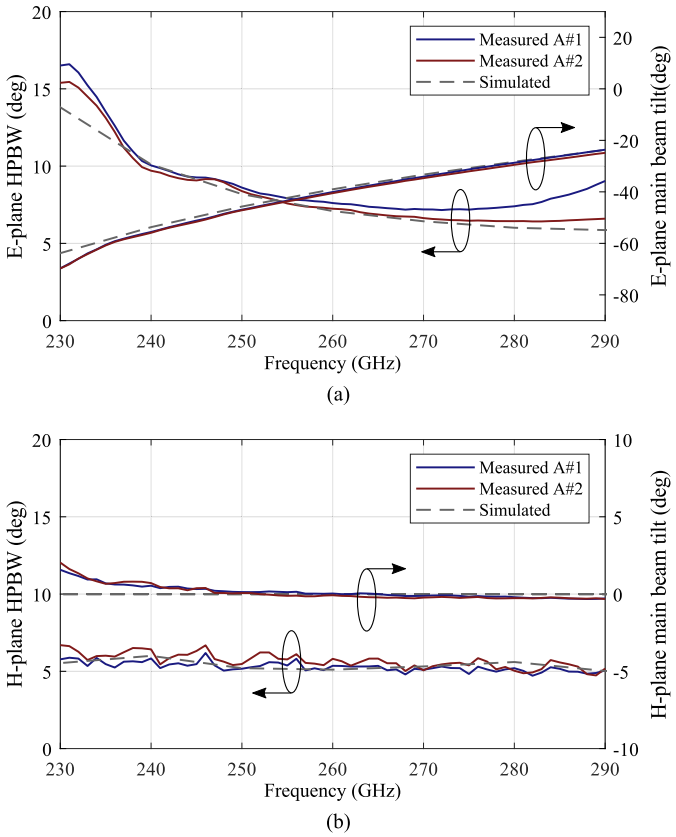

Fig. 16. Measured (solid lines) and simulated (dashed lines) half power beam width (left axis) and main beam pointing angle (right axis) for the (a) E-plane cut and (b) H-plane cut.

In the measured E-plane cuts the main beam scans from −75° at 230 GHz to -30° at 290 GHz. The H-plane cuts are always aligned with the main beam pointing direction, and the SLL is kept below 20 dB as designed. Some minor discrepancies have to be noticed on the side lobe level in the E-plane, and the HPBW at 230 GHz appears to be much larger than expected, as shown in Fig. 16. These pattern shape differences coupled with the slight shift between E-plane main beam pointing angle and half-power beam-width, indicate that the propagation losses might be slightly underestimated. At the same time, these discrepancies in both extremes of the band could be due to the difficulty of measuring antenna radiation diagrams at angles approaching backfire. In fact, at these angles, several sources of diffraction can affect the radiation pattern: effects associated to the feeding of the antenna (pin dolls; plastic screw; waveguide flange); or effects associated to the absorbing material placed behind the AUT and oversized considering the AUT dimensions. Misalignment between the two antennas can be another source of error, which is difficult to assess especially at these high frequencies.

The realised gain and the radiation efficiency for both antenna prototypes is plotted in Fig. 17. The differences noticed between the radiation patterns obtained in measurement and simulation are expressed as well in these gain results deviations. The maximum deviation between the measured and simulated insertion loss of the antenna is below 1 dB for both antennas in the whole operation band, giving an average radiation efficiency of −1 dB with a −1.9 dB worst case.

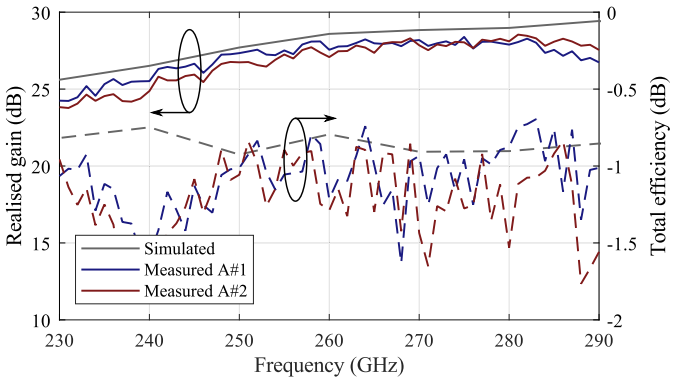

Fig. 17. Realized gain (solid lines) and radiation efficiency (dashed line) of both antenna prototypes compared to the simulated values.

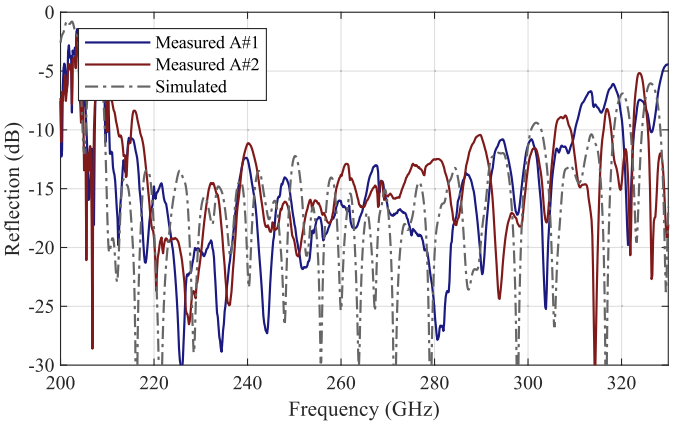

Fig. 18. Measured (solid lines) and simulated (dashed line) reflection coefficient for both antenna prototypes.

The measured and simulated reflection coefficient in Fig. 18 are below −10 dB for the 220–300 GHz antenna bandwidth. Low reflection levels are relatively challenging to obtain at these high frequencies, since any small deviation in feature sizes can have a strong effect on them. The good agreement between the measured and simulated data as well as between the two prototypes also proves the high accuracy and uniformity that silicon micromachining provides.

A summary of state of the art high gain antennas at sub-THz frequencies is shown in Table II. The table compares the performance of the most relevant work to the authors knowledge. Very little work has been published on beam-steering antennas above 100 GHz, and silicon micromachining can be identified in this comparison as a very promising manufacturing technique for this frequency range.

V. Conclusion

A silicon micromachined low profile and high gain antenna is reported in this paper. The antenna is based on a PPW leaky-wave antenna fed by a pillbox *quasi*-optical BFN. Hollow PPW pillbox structures are challenging to fabricate as frequency approaches the THz region and this work is, to the best of our knowledge, the first implementation of such system above 100 GHz.

The antenna generates a frequency steered pencil shaped beam in elevation, and further work can extend its operation

to 2-D beam steering, also in azimuth, by feeding the reflector with several input ports. Another possible improvement would be to include a more advanced tapering structure in the slots of the antenna to maximize both the aperture efficiency and the radiation efficiency.

The antenna presented here excels due to its high radiation efficiency, high gain, compact size, and large scanning range over a wide bandwidth. Its high performance, together with the batch production capabilities of silicon micromachining, makes this antenna a low cost enabling solution for several applications in the sub-THz region, including radar or beyond 5G communications.

REFERENCES

[1] G. Chattopadhyay, T. Reck, C. Lee, and C. Jung-Kubiak, "Micromachined packaging for terahertz systems," *Proc. IEEE*, vol. 105, no. 6, pp. 1139–1150, Jun. 2017.

[2] N. S. Barker, M. Bauwens, A. Lichtenberger, and R. Weikle, "Silicon-on-insulator substrates as a micromachining platform for advanced terahertz circuits," *Proc. IEEE*, vol. 105, no. 6, pp. 1105–1120, Jun. 2017.

[3] K. B. Cooper, "Imaging, Doppler, and spectroscopic radars from 95 to 700 GHz," *Proc. SPIE*, vol. 9830, pp. 983005-1–983005-9, May 2016.

[4] K. B. Cooper, R. J. Dengler, N. Llombart, B. Thomas, G. Chattopadhyay, and P. H. Siegel, "THz imaging radar for standoff personnel screening," *IEEE Trans. THz Sci. Technol.*, vol. 1, no. 1, pp. 169–182, Sep. 2011.

[5] J. Grajal *et al.*, "3-D high-resolution imaging radar at 300 GHz with enhanced FoV," *IEEE Trans. Microw. Theory Techn.*, vol. 63, no. 3, pp. 1097–1107, Mar. 2015.

[6] H. J. Gibson, B. Thomas, L. Rolo, M. C. Wiedner, A. E. Maestrini, and P. de Maagt, "A novel spline-profile diagonal horn suitable for integration into THz split-block components," *IEEE Trans. THz Sci. Technol.*, vol. 7, no. 6, pp. 657–663, Nov. 2017.

[7] N. Chahat, T. J. Reck, C. Jung-Kubiak, T. Nguyen, R. Sauleau, and G. Chattopadhyay, "1.9-THz multiflare angle horn optimization for space instruments," *IEEE Trans. THz Sci. Technol.*, vol. 5, no. 6, pp. 914–921, Nov. 2015.

[8] B. Maffei *et al.*, "High performance WR-1.5 corrugated horn based on stacked rings," *Proc. SPIE*, vol. 9153, pp. 91532W-1–91532W-9, Jul. 2014.

[9] A. V. Boriskin, R. Sauleau, J. R. Costa, and C. Fernandes, "Integrated lens antennas," in *Aperture Antennas for Millimeter and Sub-Millimeter Wave Applications*, A. V. Boriskin and R. Sauleau, Eds. New York, NY, USA: Springer, 2018, pp. 3–36.

[10] K. Konstantinidis *et al.*, "Low-THz dielectric lens antenna with integrated waveguide feed," *IEEE Trans. THz Sci. Technol.*, vol. 7, no. 5, pp. 572–581, Sep. 2017.

[11] M. Alonso-delPino, T. Reck, C. Jung-Kubiak, C. Lee, and G. Chattopadhyay, "Development of silicon micromachined microlens antennas at 1.9 THz," *IEEE Trans. THz Sci. Technol.*, vol. 7, no. 2, pp. 191–198, Mar. 2017.

[12] M. Alonso-delPino, C. Jung-Kubiak, T. Reck, N. Llombart, and G. Chattopadhyay, "Beam scanning of silicon lens antennas using integrated piezomotors at submillimeter wavelengths," *IEEE Trans. THz Sci. Technol.*, vol. 9, no. 1, pp. 47–54, Jan. 2019.

[13] K. Murano *et al.*, "Low-profile terahertz radar based on broadband leaky-wave beam steering," *IEEE Trans. THz Sci. Technol.*, vol. 7, no. 1, pp. 60–69, Jan. 2017.

[14] M. Ettorre, A. Neto, G. Gerini, and S. Maci, "Leaky-wave slot array antenna fed by a dual reflector system," *IEEE Trans. Antennas Propag.*, vol. 56, no. 10, pp. 3143–3149, Oct. 2008.

[15] T. Djerafi and K. Wu, "A low-cost wideband 77-GHz planar Butler matrix in SIW technology," *IEEE Trans. Antennas Propag.*, vol. 60, no. 10, pp. 4949–4954, Oct. 2012.

[16] M. Ettorre, R. Sauleau, L. L. Coq, and F. Bodereau, "Single-folded leaky-wave antennas for automotive radars at 77 GHz," *IEEE Antennas Wireless Propag. Lett.*, vol. 9, pp. 859–862, 2010.

[17] F. Foglia Manzillo *et al.*, "A wide-angle scanning switched-beam antenna system in LTCC technology with high beam crossing levels for V-band communications," *IEEE Trans. Antennas Propag.*, vol. 67, no. 1, pp. 541–553, Jan. 2019.

[18] T. Potelon *et al.*, "A low-profile broadband 32-slot continuous transverse stub array for backhaul applications in *E*-band," *IEEE Trans. Antennas Propag.*, vol. 65, no. 12, pp. 6307–6316, Dec. 2017.

[19] K. Fan, Z.-C. Hao, Q. Yuan, and W. Hong, "Development of a high gain 325–500 GHz antenna using quasi-planar reflectors," *IEEE Trans. Antennas Propag.*, vol. 65, no. 7, pp. 3384–3391, Jul. 2017.

[20] W. Rotman, "Wide-angle scanning with microwave double-layer pillboxes," *IRE Trans. Antennas Propag.*, vol. 6, no. 1, pp. 96–105, Jan. 1958.

[21] B. Beuerle, J. Campion, U. Shah, and J. Oberhammer, "A very low loss 220–325 GHz silicon micromachined waveguide technology," *IEEE Trans. THz Sci. Technol.*, vol. 8, no. 2, pp. 248–250, Mar. 2018.

[22] T. J. Reck, C. Jung-Kubiak, J. Gill, and G. Chattopadhyay, "Measurement of silicon micromachined waveguide components at 500–750 GHz," *IEEE Trans. THz Sci. Technol.*, vol. 4, no. 1, pp. 33–38, Jan. 2014.

[23] A. Gomez-Torrent, U. Shah, and J. Oberhammer, "Compact silicon-micromachined wideband 220–330-GHz turnstile orthomode transducer," *IEEE Trans. THz Sci. Technol.*, vol. 9, no. 1, pp. 38–46, Jan. 2019.

[24] K. Tekkouk *et al.*, "Corporate-feed slotted waveguide array antenna in the 350-GHz band by silicon process," *IEEE Trans. Antennas Propag.*, vol. 65, no. 1, pp. 217–225, Jan. 2017.

[25] K. Sarabandi, A. Jam, M. Vahidpour, and J. East, "A novel frequency beam-steering antenna array for submillimeter-wave applications," *IEEE Trans. THz Sci. Technol.*, vol. 8, no. 6, pp. 654–665, Nov. 2018.

[26] A. A. Oliner, "Leaky-wave antennas," in *Antenna Engineering Handbook*, R. C. Johnson, Ed. New York, NY, USA: McGraw-Hill, 1992, pp. 280–338.

[27] J. Campion, U. Shah, and J. Oberhammer, "Elliptical alignment holes enabling accurate direct assembly of micro-chips to standard waveguide flanges at sub-THz frequencies," in *IEEE MTT-S Int. Microw. Symp. Dig.*, Jun. 2017, pp. 1262–1265.

[28] A. R. Conn, N. I. M. Gould, and P. L. Toint, *Trust Region Methods*, vol. 1. Philadelphia, PA, USA: SIAM, 2000.

Adrian Gomez-Torrent (GS'18) was born in Artariáin, Spain, in 1990. He received the B.Sc. and M.Sc. degrees from the Public University of Navarra (UPNA), Pamplona, Spain, in 2014.

From 2013 to 2017, he was with the Antennas and Microwave Components Groups, UPNA, where he was involved with microwave passive devices and silicon micromachining for RF/THz components. Since 2017, he has been with the Division of Micro and Nanosystems, Kungliga Tekniska Högskolan (KTH) Royal Institute of Technology, Stockholm, Sweden. His current research interests include silicon micromachining for microwave and subTHz passive waveguide components, antennas, and switching networks for beam-steering applications.

María García-Vigueras received the M.Sc. degree in telecommunications engineering and the Ph.D. degree from the Technical University of Cartagena, Cartagena, Spain, in 2007 and 2012, respectively.

From 2012 to 2015, she was a Research Fellow with the Laboratory of Electromagnetism and Antennas, École Polytechnique Fédéral de Lausanne, Lausanne, Switzerland. She is currently an Assistant Professor with the Institut National des Sciences Appliquées de Rennes, Rennes, France. She has coauthored more than 15 IEEE journals and 40 publications in international conferences. Her current research interests include leaky wave antennas, periodic surfaces, waveguide feed chain components, and the evaluation of additive manufacturing's potential for RF design.

Dr. García-Vigueras was a recipient of several prizes, including two Best Ph.D. Thesis Awards from COIT/AEIT in 2014 and UPCT in 2013, respectively, in Spain, the Best Paper Awards in China, and the EuCAP 2012 Award in Prague.

Laurent Le Coq received the degree in electronic engineering and radiocommunications, the french DEA (M.Sc.) degree in electronics, and the Ph.D. degree from the National Institute of Applied Science (INSA), Rennes, in 1995 and 1999, respectively.

In 1999, he joined the Institute of Electronics and Telecommunications of Rennes (IETR), University of Rennes 1, Rennes, as a Research Lab Engineer, responsible of antenna centi- and milli-meter wave range test facilities. Since 2018, he has been the Scientific Manager of manufacturing measurement and analysis of radiating systems (M2ARS) with the IETR Facility Unit, bringing together seven facilities dedicated to Electro Magnetic studies up to 500 GHz, among which three antenna test and imaging facilities (up to 300 GHz) and a prototyping service. His activities in antenna measurements and development of related procedures involved him in more than 30 research contracts of national or European interest. He has authored or coauthored more than 50 journal articles and 50 papers in conference proceedings.

Adham Mahmoud, photograph and biography not available at the time of publication.

Mauro Ettorre (M'08–SM'15) received the Laurea degree *(summa cum laude)* in electrical engineering and the Ph.D. degree in electromagnetics from the University of Siena, Siena, Italy, in 2004 and 2008, respectively. Part of his Ph.D. work was developed at the Netherlands Organisation for Applied Scientific Research (TNO), The Hague, The Netherlands.

He was an Antenna Researcher with TNO. From 2008 to 2010, he was a Post-Doctoral Fellow with the Institut d'Electronique et de Télécommunications de Rennes (IETR), University of Rennes 1, Rennes, France. In 2010 and 2016, he was a Visiting Scholar with the Radiation Laboratory, Department of Electrical Engineering and Computer Science, University of Michigan, Ann Arbor, MI, USA. Since October 2010, he has been a Research Scientist with the Centre National de la Recherche Scientifique (CNRS), IETR. In 2014, he assumed responsibilities for the multi-beam antenna activity for satellite applications in the joint laboratory between IETR and Thales Alenia Space, Toulouse, France. In 2015, he was an Invited Professor with the Tokyo Institute of Technology (TIT), Tokyo, Japan. Since 2016, he has been the Secretary of the French National Committee for Scientific Research, Section 08 (micro- and nanotechnologies, photonics, electromagnetism), CNRS, Paris, France. His current research interests include the analysis and design of leaky-wave antennas, periodic structures, millimeter-wave antennas, nondiffractive radiation and localized waves, near-field focusing techniques, and wireless power transfer systems.

Dr. Ettorre was a member of the Best Paper Award Selection Committee of the IEEE TRANSACTIONS ON TERAHERTZ SCIENCE AND TECHNOLOGY, in 2017, 2018, and 2019. He was a recipient of the Young Antenna Engineer Prize from the 2008 ESA Antenna Workshop, The Netherlands, the Innovation Award from the 2018 ESA Antenna Workshop, The Netherlands, and the Best Paper Award in Electromagnetics and Antenna Theory from the 2018 European Conference on Antennas and Propagation (EuCAP), London, U.K. Since 2017, he has been an Associate Editor of the IEEE TRANSACTIONS ON ANTENNAS AND PROPAGATION.

Ronan Sauleau (M'04–SM'06–F'18) received the M.Sc. degree in electrical engineering and radio communications from the Institut National des Sciences Appliquées de Rennes, Rennes, France, in 1995, the Agrégation degree from the École Normale Supérieure de Cachan, Cachan, France, in 1996, and the Ph.D. degree in signal processing and telecommunications and the Habilitation à Diriger des Recherches degree from the University of Rennes 1, Rennes, in 1999 and 2005, respectively.

From 2000 to 2005 and from 2005 to 2009, he was an Assistant Professor and an Associate Professor with the University of Rennes 1, respectively, where he has been a Full Professor since 2009. He is currently the Co-Director of the Department of Antenna and Microwave Devices, Institut d'Electronique et de Télecommunications de Rennes (IETR), Rennes, where he is also the Deputy Director. He has shared the responsibility of the research activities on antennas at IETR in 2010 and 2011. He has been involved in more than 35 research projects at the national and European levels and has co-supervised 20 post-doctoral fellows, 35 Ph.D. students, and 50 master's students. He has authored or coauthored more than 195 journal articles and 410 publications in international conferences and workshops. He holds 14 patents. His current research interests include numerical modeling (mainly FDTD), millimeter-wave printed and reconfigurable antennas, substrate-integrated waveguide antennas, lens-based focusing devices, periodic and nonperiodic structures (electromagnetic bandgap materials, metamaterials, reflectarrays, and transmitarrays), and biological effects of millimeter waves.

Dr. Sauleau was elevated to a Junior Member of the Institut Universitaire de France in 2007. He is a member of the Board of Directors of EurAAP. He was a recipient of the 2004 ISAP Conference Young Researcher Scientist Fellowship, Japan, the first Young Researcher Prize in Brittany, France, in 2001, for his research work on gain-enhanced Fabry–Perot antennas, and the Bronze Medal by CNRS in 2008. He was a co-recipient of several international conference awards with some of his students (Int. Sch. of BioEM 2005, BEMS'2006, MRRS'2008, E-MRS'2011, BEMS'2011, IMS'2012, Antem'2012, and BioEM'2015). He served as a Guest Editor for the IEEE TRANSACTIONS ON ANTENNAS AND PROPAGATION Special Issue on Antennas and Propagation at mm and sub mm Waves. He served as a National Delegate for COST VISTA. Since 2013, he has been a National Delegate for EurAAP.

Joachim Oberhammer (M'06–SM'12) was born in Brunico, Italy, in 1976. He received the M.Sc. degree in electrical engineering from the Graz University of Technology, Graz, Austria, in 2000, and the Ph.D. degree from the Kungliga Tekniska Högskolan (KTH) Royal Institute of Technology, Stockholm, Sweden, in 2004.

He was a Post-Doctoral Research Fellow with Nanyang Technological University, Singapore, in 2004, and Kyoto University, Kyoto, Japan, in 2008. Since 2005, he has been leading radio-frequency/microwave/terahertz microelectromechanical systems research at the KTH Royal Institute of Technology; has been an Associate Professor with the KTH Royal Institute of Technology since 2010; and has also been a Professor of microwave and THz microsystems with the KTH Royal Institute of Technology since 2015. He was a Guest Researcher with Nanyang Technological University in 2007 and with the NASA Jet Propulsion Laboratory, Pasadena, CA, USA, in 2014. He has authored or coauthored more than 100 reviewed research articles and holds four patents.

Dr. Oberhammer served as a TPRC member for IEEE Transducers 2009 and 2015, the IEEE International Microwave Symposiums 2010–2016, the IEEE Micro Electro Mechanical Systems 2011 and 2012, and the IEEE Radio and Wireless Week 2015 and 2016. He has been a Steering Group Member of the IEEE MTT-S and AP-S Chapters Sweden since 2009. In 2013, he received an ERC Consolidator Grant by the European Research Council. Since 2014, he has been a Steering Group Member of the Young Academy of Sweden. He was a recipient of the Award by the Ericsson Research Foundation, a grant by the Swedish Innovation Bridge, and a scholarship by the Japanese Society for the Promotion of Science, in 2004, 2007, and 2008, respectively. The research work, his heading received six Best Paper Awards (five of which at IEEE conferences) and four IEEE Graduate Fellowship Awards (by the IEEE MTT-S and by AP-S) since 2009.